High-efficiency perovskite-polymer bulk heterostructure light-emitting diodes

Baodan Zhao[1], Sai Bai[2,3], Vincent Kim[1], Robin Lamboll[1], Ravichandran Shivanna[1], Florian Auras[1], Johannes M. Richter[1], Le Yang[1,4], Linjie Dai[1], Mejd Alsari[1], Xiao-Jian She[1], Lusheng Liang[5], Jiangbin Zhang[1], Samuele Lilliu[6,7], Peng Gao[5], Henry J. Snaith[2], Jianpu Wang[8], Neil C. Greenham[1], Richard H. Friend[1]* & Dawei Di[1]*

1. Cavendish Laboratory, Cambridge University, JJ Thomson Avenue, Cambridge, CB3 0HE, UK
2. Department of Physics, University of Oxford, Clarendon Laboratory, Oxford, OX1 3PU, UK
3. Department of Physics, Chemistry and Biology (IFM), Linköping University, Linköping, SE-581 83, Sweden
4. Institute of Materials Research and Engineering (IMRE), Agency for Science, Technology and Research (A*STAR), 2 Fusionopolis Way, Singapore 138634, Singapore
5. Laboratory of Advanced Functional Materials, Xiamen Institute of Rare Earth Materials, Haixi Institute, Chinese Academy of Sciences, Xiamen 361021, China
6. Department of Physics and Astronomy, University of Sheffield, Sheffield, S3 7RH, UK
7. The UAE Centre for Crystallography, United Arab Emirates
8. Institute of Advanced Materials (IAM), Nanjing Tech University, 30 South Puzhu Road, Nanjing, 211816, China

Perovskite-based optoelectronic devices are gaining significant attention owing to their remarkable performance and low processing cost, particularly for solar cells. However, for perovskite light-emitting diodes (LEDs), non-radiative charge recombination has limited the electroluminescence (EL) efficiency. Here we demonstrate perovskite-polymer bulk heterostructure LEDs exhibiting external quantum efficiencies (EQEs) of up to 20.1% (at current densities of 0.1-1 mA cm^{-2}). The LED emissive layer comprises quasi-2D/3D perovskites and an insulating polymer. Photogenerated excitations migrate from quasi-2D to lower-energy sites within 1 ps, followed by radiative bimolecular recombination in the 3D regions. From near-unity external PL quantum efficiencies and transient kinetics of the emissive layer with/without charge-transport contacts, we find non-radiative recombination pathways to be effectively eliminated, consistent with optical models giving near-100% internal quantum efficiencies (IQEs). Although device brightness and stability (T_{50} = 46 h in air at peak EQE) require further improvements, our results indicate the significant potential of perovskite-based photon sources.

The rapid advance of perovskite solar cells[1–4] has prompted the development of other types of perovskite-based optoelectronics, including LEDs[5–8], lasers[9,10] and photo-detectors[11,12]. Similar to conventional semiconductors, the luminescence efficiency of photo- or electrically-excited charge carriers in perovskite materials is governed by the relative strengths of radiative and non-radiative processes. Since the first report of halide perovskite LEDs in 2014[5], the device EQEs have risen from below 1%[5] to ~14%[13]. While these high EL efficiencies are surprising for the solution-processed hybrid semiconductor containing a considerable level of grain-boundary and interfacial defects, such device performance still falls behind that of the best OLEDs[14–16] which exhibit EQEs of more than 20% without enhanced optical outcoupling. Despite the good tolerance of the hybrid perovskite materials family to electronic defects[17], the EL efficiencies achieved to date suggest that the

suppression of non-radiative recombination under electrical excitation conditions still remains a challenge. Non-radiative recombination is also an important mechanism for voltage loss in photovoltaic solar cells[18]. An ideal open-circuit voltage predicted by the Shockley-Queisser model[19] is only achievable with near-unity luminescence yield[20]. To enhance radiative emission processes in LEDs, one of the most successful approaches reported so far is the use of low-dimensional structures such as nanocrystals[21–23] and quasi-2D/3D nanostructures[7,8] that are considered to confine charge carriers.

Perovskite-polymer bulk heterostructure

In this work, we explore the optoelectronic and photophysical properties of a perovskite-polymer bulk heterostructure (PPBH). The emissive heterostructure is prepared from a combination of quasi-2D/3D perovskites and a wide optical gap (E_g = 4.96 eV) polymer, poly(2-hydroxyethyl methacrylate) (poly-HEMA) (Supplementary Fig. 1). The weight ratio of the PPBH precursors, 1-naphthylmethylammonium iodide (NMAI), formamidinium iodide (FAI), lead iodide (PbI_2), and the poly-HEMA, in the precursor solution is 5:3:8:4 (the weight fraction of the polymer in the precursors is 20%). The volume fractions of the perovskite phase and the polymer phase in the resultant PPBH film are estimated to be 72% and 28%, respectively (Methods). The absorption profile of the PPBH contains a distinct excitonic peak at ~575 nm, corresponding to the quasi-2D perovskite with a formula of $(NMA)_2(FA)Pb_2I_7$ (Fig. 1a and Supplementary Fig. 2a). The absorption tail of the PPBH sample extends to ~800 nm, which we attribute to the presence of a small fraction of quasi-3D $(NMA)_2(FA)_{m-1}Pb_mI_{3m+1}$ ($m >> 1$) phase. The photoluminescence (PL) spectrum of the sample peaks at ~795 nm (~1.56 eV), with a full-width-at-half-maximum (FWHM) of ~55 nm. Grazing-incidence wide-angle X-ray scattering (GIWAXS) measurements indicate that the perovskite crystallites are isotropically oriented in the PPBH film (Fig. 1b). High-resolution transmission electron microscopy (HR-TEM) results suggest the presence of quasi-2D/3D crystal structures[24] (Fig. 1c). From the X-ray diffraction (XRD) data, the average crystallite size is estimated to be 30-55 nm based on the FWHM of the diffraction peaks (Supplementary Fig. 2a). The average surface roughness of the film is ~3.3 nm (Supplementary Fig. 2c).

Structure and performance of PPBH LEDs

To investigate the electroluminescence (EL) properties of the PPBH, we developed a solution-processed multilayer LED structure (Methods) (Fig. 1d). The electron-transport/hole-blocking layer (ETL/HBL) is formed by a 20-nm thick spin-coated layer of magnesium-alloyed zinc oxide (MZO), a tunable wide-bandgap n-type metal oxide, formed on indium tin oxide (ITO)-coated glass. A polyethylenimine (PEIE) interlayer is then formed on the MZO layer, followed by the PPBH emissive layer (180 nm). A 50-nm layer of poly(9,9-dioctylfluorene-alt-N-(4-sec-butylphenyl)-diphenylamine) (TFB) blended with poly(9,9-di-n-octylfluorenyl-2,7-diyl) (PFO) (at a weight ratio of 4:1) is then spin-coated on top of the PPBH layer from toluene solution. The TFB-PFO polymer blend serves as a tunable hole-transport/electron-blocking layer (HTL/EBL).

The EL spectrum of the PPBH LED is nearly identical to that of the steady-state PL (Supplementary Fig. 2d), exhibiting a slightly narrower FWHM of ~49 nm. The low onset of radiance (10^{-4} W sr^{-1} m^{-2} at 1.3 V) indicates that the LED structure allows barrier-free bi-polar charge injection into the emissive layer (Fig. 2a). The peak EQE of best devices reaches 20.1% (Fig. 2b, c),

representing a record for perovskite-based LEDs (Fig. 2d)[5–8,22,25]. The angle-dependent EL intensities exhibit a Lambertian profile (Supplementary Fig. 3a), allowing accurate estimation of EQEs. As the drive voltages are low, the wall-plug efficiency (electricity-to-light power-conversion efficiency) is also high, reaching 16.2% (Supplementary Fig. 3b). The efficiencies of our perovskite-based LEDs are on par with those of the best OLEDs[14–16] and quantum-dot (QD) LEDs[26]. For devices encapsulated in epoxy adhesive/cover glass, the EL half-life in air under continuous operation at the current density corresponding to the peak EQE point (0.1 mA cm^{-2}) has reached 46 hours (Fig. 2e). Further improvements are required for practical applications.

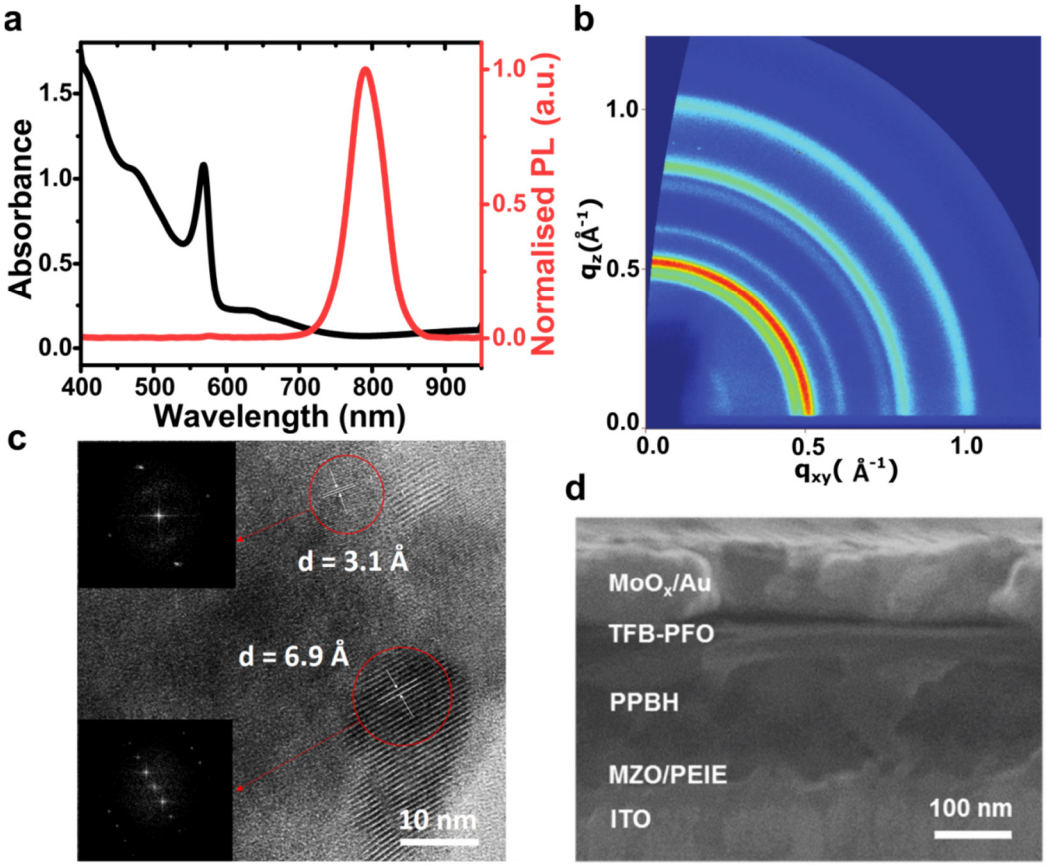

Figure 1 | Basic optical and structural characterisation of PPBH. a, Absorbance (black) and PL (red) spectra of a PPBH film on fused silica. **b**, GIWAXS patterns of a PPBH layer deposited on silicon. **c**, HR-TEM image of a PPBH sample. Insets show the fast Fourier transforms of the quasi-2D/3D crystalline regions. **d**, Cross-sectional scanning electron microscopy (SEM) image of the LED structure.

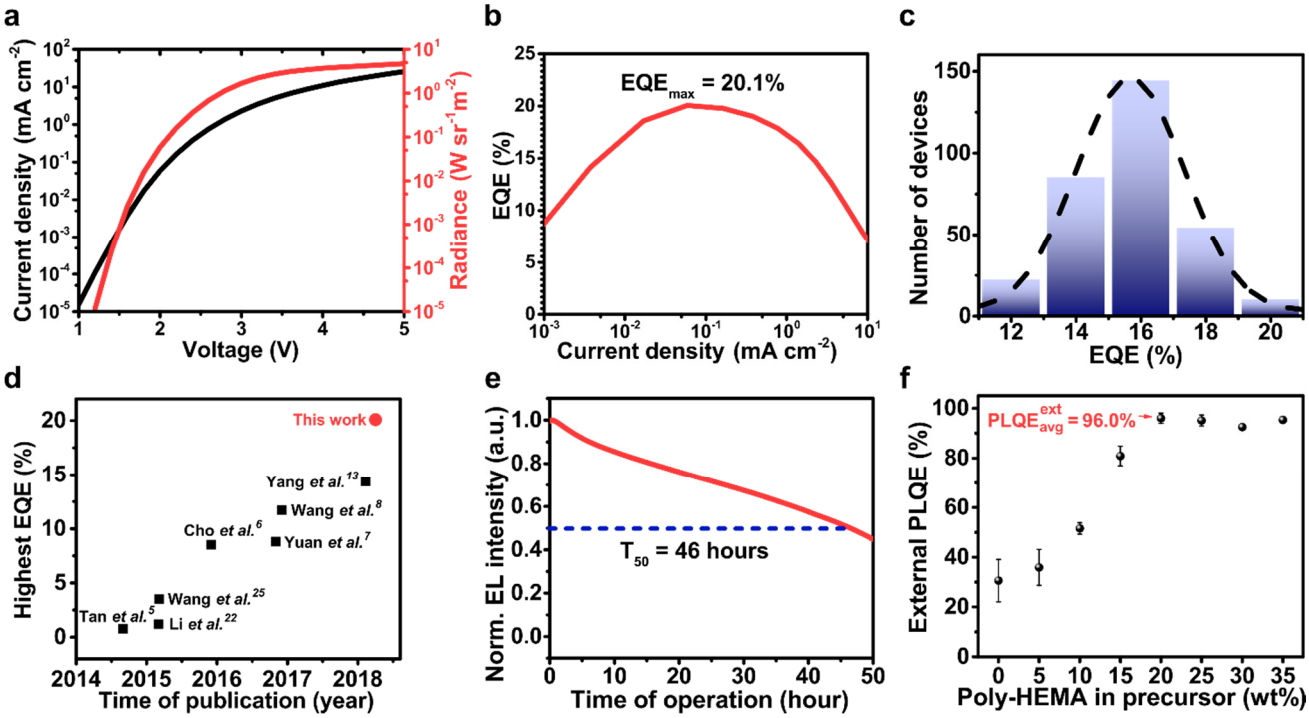

Figure 2 | LED performance characterisation and emissive layer PLQEs. a, Current-voltage and radiance-voltage characteristics. **b**, EQE-current density characteristics of the best PPBH LED (peak EQE = 20.1%). **c,** Peak EQE histogram of 320 devices. **d,** Development of halide perovskite-based LEDs. Note: Ref 13 was published during the revision of this paper. **e,** Operational stability measurement of PPBH LEDs, performed in air at a constant current density corresponding to the peak EQE point (0.1 mA cm^{-2}). **f,** External PLQE of PPBH films (on fused silica) as a function of poly-HEMA weight fraction in the solid precursors. The optimised polymer weight fraction of 20% in precursor corresponds to a volume fraction of 28% in the PPBH film. The excitation source used was a 532-nm CW laser with an intensity of 100 mW cm^{-2} (approximately one-sun).

Transient luminescence kinetics

For films of PPBH (thickness: ~180 nm) deposited on fused silica substrates, we observe external PL quantum efficiencies (PLQEs) of 90±10% under 532-nm steady-state excitation (10-300 mW cm^{-2}) using an integrating sphere (Methods). The external PLQE is 96±3% for optimised PPBH films under 100 mW cm^{-2} (approximately one-sun) excitation (Fig. 2f). To translate the high PLQE into good EL efficiency, a key consideration is the prevention of luminescence quenching at the charge-transport interfaces, as interfacial states often create non-radiative pathways, imposing severe limitations on optoelectronic performance[27]. Accurate assessment of PLQE of the emissive layer in an LED structure using an integrating sphere is limited by the parasitic absorption of charge-transport layers and electrodes. Therefore, we employ a range of transient optical spectroscopy techniques in this work to investigate excitation and recombination processes in the PPBH system. We find that the charge-transport layers have no observable effect on the PL decay kinetics of the PPBH emissive layer (Fig. 3a,b), indicating that non-radiative recombination events at the two contact interfaces are insignificant. In contrast, for identically-prepared quasi-2D/3D perovskite films without the polymer component, bulk and interfacial luminescence quenching processes are clearly present (Supplementary Fig. 4a-c). We do not observe any evidence for additional non-radiative decay processes from the transient EL profile (Supplementary Fig. 4d).

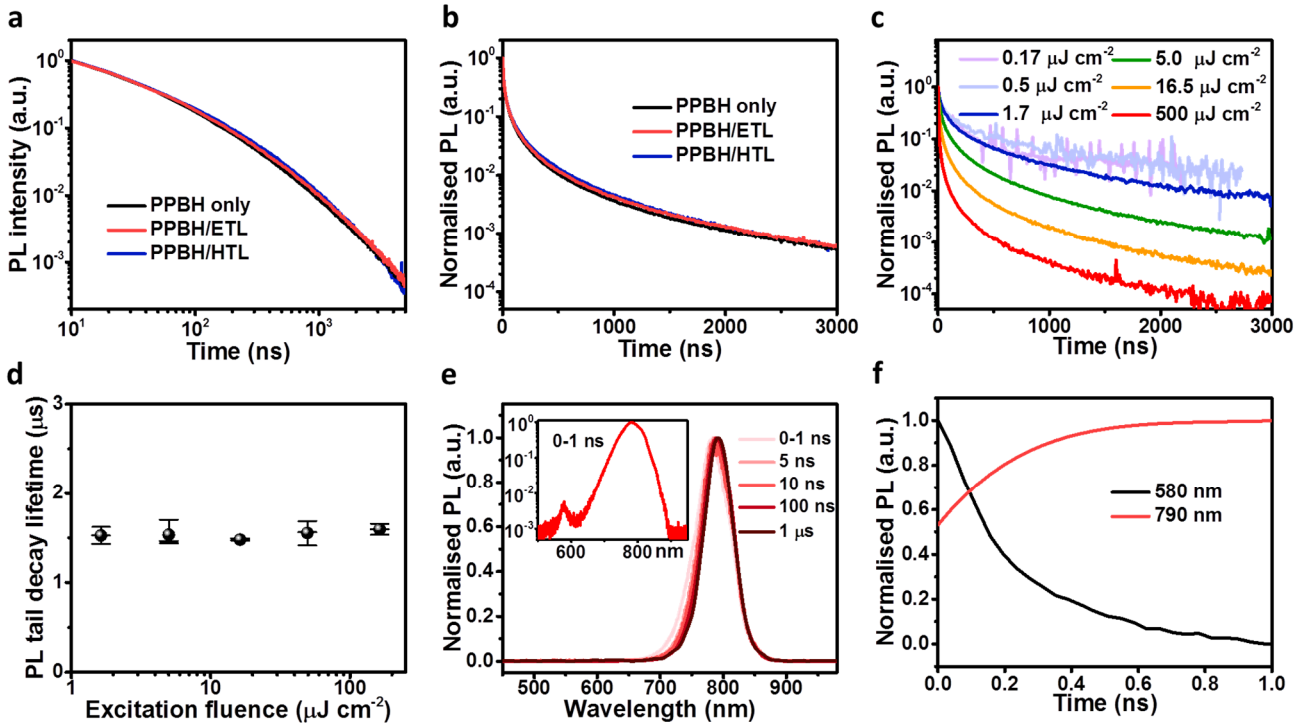

Figure 3 | Transient (ns-μs) optical experiments. a, PL kinetics of a PPBH film and identical PPBH samples with charge-transport layers, plotted on log-log scale for 680-900 nm emission. **b**, PL kinetics of a PPBH film and identical PPBH samples with charge-transport layers, plotted on log-linear scales for 680-900 nm emission. **c**, Excitation-intensity-dependent PL kinetics of a PPBH film. The initial intensities of all PL decay trances are normalised to 1 at t = 0. **d**, PL decay tail lifetime as a function of excitation intensity. **e**, ns-μs time-resolved PL spectra. The excitation source for the PL experiments in Fig. 3a-e was a 400-nm, 80-fs pulsed laser with a repetition frequency of 1 kHz. Unless otherwise specified, the excitation fluence of the PL measurements was 5 μJ cm^{-2}. An intensified CCD (iCCD) system with a temporal resolution of ~2 ns was used. **f**, Instrumentally-limited kinetics of the short (~580 nm) and long (~790 nm) wavelength PL components measured by time-correlated single photon counting (TCSPC). The excitation source was a 407-nm laser with a pulse width of < 200 ps. The temporal resolution of the setup is ~0.2 ns.

The excitation-fluence-dependent PL decay profiles of the PPBH sample from 0 ns to 3 μs at 10-ns time-steps are shown in Fig. 3c. The PL decay kinetics show a significant dependence on excitation intensity, consistent with the view that in the emissive layer, the carrier recombination rate can be understood by a superposition of first-order (monomolecular), second-order (bimolecular) and higher-order processes, as has been discussed in earlier reports[9,28,29]. The early-time emission process in the PPBH system is dominated by an energy-migration process (*vide infra*), and hence deviates from this model.

We find that for the PL process at 5 ns < t < 1 μs, which accounts for ~90% of the total emission for excitation fluences greater than 1.7 μJ cm^{-2}, the decay kinetics can be approximately described by a bimolecular process. At later times (t > 1 μs), when the carrier density in the system is low, the PL decays follow a mono-exponential process. The lifetimes of these PL decay tails are approximately 1.5 μs for a range of excitation intensities (Fig. 3d). This lifetime is an indication of trap-assisted non-radiative recombination lifetime of photoexcitations at low carrier densities, or the intrinsic decay lifetime of weakly bound electron-hole pairs in the PPBH.

From the ns-µs PL spectra of the PPBH (Fig. 3e), we observed that the PL profile stablised to the steady-state PL after $t > 10$ ns, following an initial spectral redshift. At early times ($t < 1$ ns), a weak PL contribution from the quasi-2D perovskite was observed. Accurate determination of the decay and rise times of the high- (~580 nm) and low-energy (~790 nm) emissive species was limited by the temporal response (0.2 ns) of the experimental setup (Fig. 3f) (Methods). Ultrafast PL experiments in the fs-ps time-range (Fig. 4a) show that photoexcitation at 400 nm to mostly the quasi-2D perovskite gives early-time emission from these regions (peaked at ~580 nm), with a characteristic lifetime of ~10 ps (Fig. 4b), and is insensitive to excitation intensity (Supplementary Fig. 5a,b). The fs-ps PL kinetics of the longer-wavelength (> 680 nm) component could not be recorded by our ultrafast PL setup due to the limited spectral detection window[16].

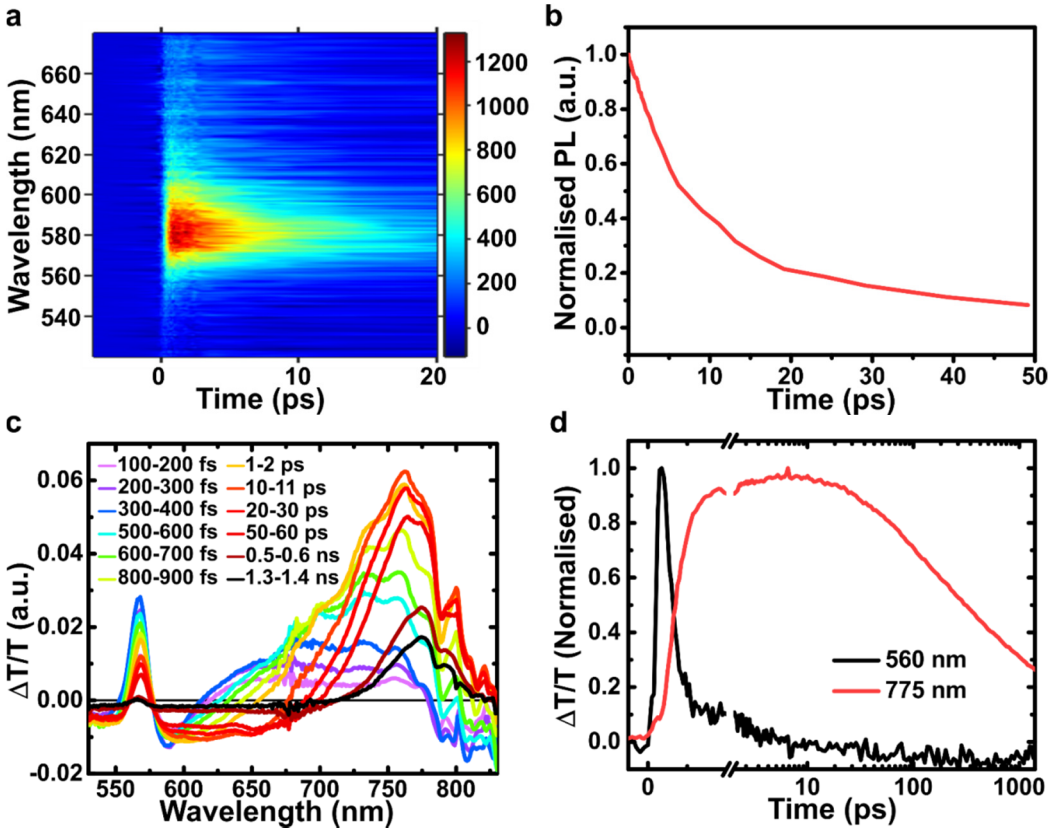

Figure 4 | Ultrafast (fs-ps) transient optical experiments. a, Ultrafast (ps) PL spectra. The excitation fluence used was 5 µJ cm^{-2}. **b**, Ultrafast (ps) PL decay kinetics at 550-620 nm. **c**, Transient absorption (TA) spectra of the sample. The excitation fluence for the TA measurement was 16 µJ cm^{-2}. **d**, TA kinetics of the high- and low-energy absorption species. For all ultrafast optical measurements, the excitation source was a 400-nm, 80-fs pulsed laser with a repetition rate of 1 kHz.

Transient absorption kinetics

Transient absorption (TA) experiments (Fig. 4c) confirm that the initial photoexcitation is formed on the quasi-2D perovskite, with a ground-state bleach (GSB) peak at ~575 nm. The peak position is in agreement with the steady-state absorption and transient PL measurements. The GSB feature related to the bi-layer quasi-2D perovskite has an exciton-like character, suggesting the electron-hole pair created in the material is initially bound. As the 575-nm GSB quickly decays, a red-shifting, broad GSB signal rises rapidly and then declines after 10 ps. The kinetics of the

~575-nm and the ~775-nm processes which are related to the emissive species identified by the PL experiments are shown in Fig. 4d. The data show that the initial excitation at the 575-nm high-energy site relaxes within ~1 ps, while the remaining states with the same energy decay in ~10 ps, consistent with the ultrafast PL experiment showing a 10-ps decay time. The 1-ps rise time of the lower-energy (~775 nm) excitations suggests that the energy transfer from higher-bandgap to lower-bandgap components in the PPBH takes place within the same timeframe. Following the initial 1-ps ultrafast energy migration, the residual localised excitations at the 2-layer quasi-2D perovskite decay in ~10 ps. The majority of the excited states in the lower-bandgap components likely exist in the form of charged excitations rather than tightly-bound excitons, as implicated by the broadened GSB features of the lower-energy excitations. At later times (t > 1 ns), most of these charge carriers recombine to produce luminescence, as discussed previously in the ns-μs transient studies. Supplementary Table 1 presents a summary of key photophysical parameters extracted from our transient optical experiments.

Models of photon outcoupling

Finally, we discuss models of photon extraction from the LED structure. From a conventional optics perspective, we note that the refractive index of the PPBH system which we measure to be 1.9 at the peak of its steady-state luminescence is significantly lower than the refractive index of 2.7 for standard halide perovskites. This lower refractive index widens the escape cone of photon emission from the emissive layer to 32˚. Including the effects of interference and assuming experimentally-determined optical constants and layer thicknesses, we model an outcoupling factor of up to ~21% (Fig. 5a), depending on where in the emissive layer photons are emitted, with values of ~25% possible if emissive layer thicknesses are optimised (Fig. 5b). The similarity between modelled outcoupling factor and EQE implies near-unity IQEs, in agreement with the outstanding PL and EL properties observed. Lateral PL experiments (Fig. 5c, d and Supplementary Fig. 6) show that light initially confined as modes waveguided in PPBH layer can propagate up to 80 μm. The intense PL signal at d < 10 μm resembles the intensity profile of the excitation laser spot. The PL decay beyond 10 μm (the system resolution) has a characteristic decay profile similar to that observed previously in halide perovskites[30], indicating a possible contribution from photon recycling. Therefore, while an EQE of over 20% for PPBH LEDs can be accounted for within the conventional outcoupling model described above, photon recycling effect brings IQE closer to the measured EQE and may provide prospects of further efficiency improvements.

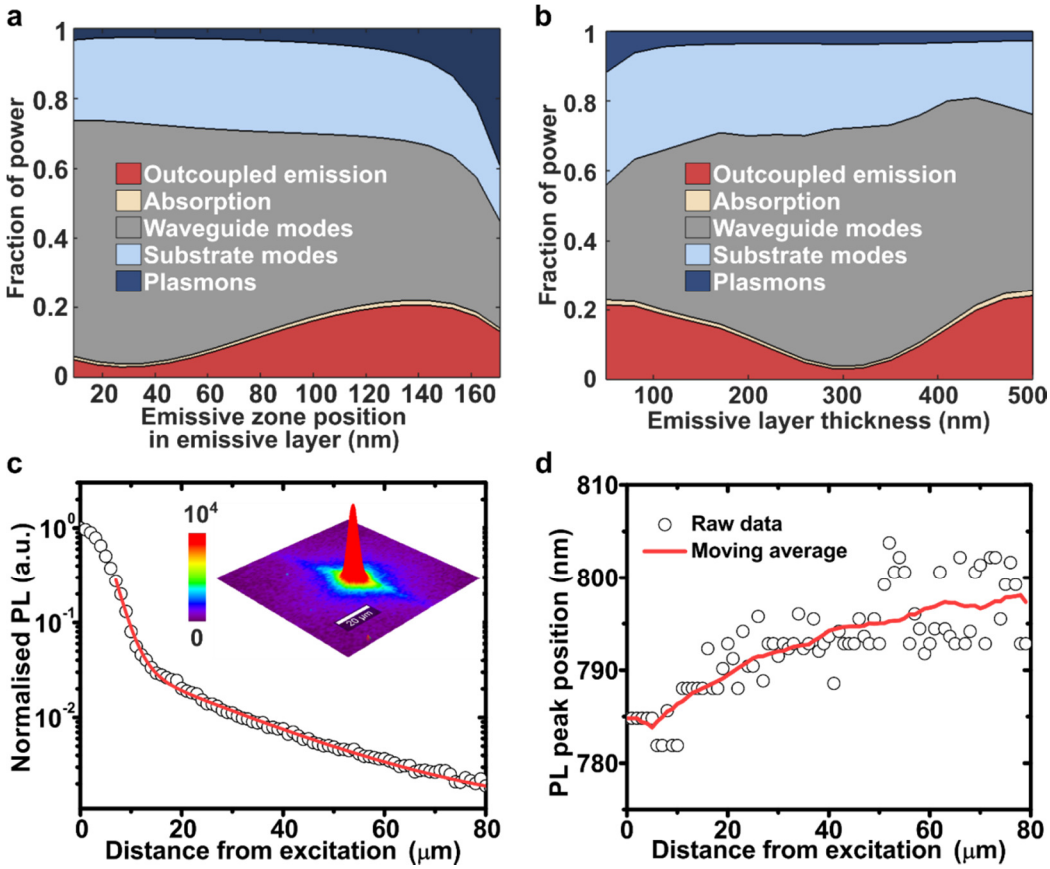

Figure 5 | Optical modelling of PPBH LEDs and lateral PL experiments. a, Modelled fractional optical power distribution in the LED structure as a function of emission zone position in the PPBH emissive layer with a thickness of 180 nm. The origin of the x-axis is the ETL/emissive layer interface. 'Outcoupled emission' indicates the fraction of out-coupled light from the LED. Other modes lead to optical losses. **b**, Modelled fractional optical power as a function of PPBH layer thickness. The emission zone is assumed to be at the centre of the emissive layer. **c**, PL intensity as a function of lateral distance from the point of excitation. **d**, PL peak position as a function of lateral distance from the point of excitation. The redshift of PL peak over distance indicates spectrum filtering (self-absorption) within the emissive layer.

Conclusions

In this work, we have demonstrated PPBH LEDs with high EQEs of up to 20.1% at 0.1-1 mA cm^{-2}. They represent the most efficient perovskite-based LEDs to date, and are comparable with some of the best OLEDs and QD LEDs[14–16,26]. The EL half-life reaches 46 hours in air at the peak EQE point (0.1 mA cm^{-2}). Further improvements are required to suit practical applications. Transient optical experiments suggest that in the PPBH system, localised higher-energy excitations dissociate into charges at lower-energy sites within ~1 ps, significantly faster than the ~100 ps energy funnelling time reported for quasi-2D/3D perovskites[7,8]. The ultrafast migration of excitations observed ensures that any non-radiative traps with energies above the final emissive species are rendered insignificant, as these loss processes need to compete kinetically with the rapid excitation transfer. After the rapid energy migration, emission occurs primarily through a bimolecular recombination channel. PPBH thin films with/without charge-transport contacts exhibit a PL decay tail (monomolecular) lifetime of ~1.5 μs, comparable to or exceeding that observed for perovskite single crystals[31,32], indicating low trap densities in these structures. Bulk and interfacial non-radiative

relaxation processes are effectively suppressed, leading to the excellent EQEs and the near-unity external PLQEs (~96% under 100 mW cm^{-2}). Optical outcoupling from the emissive layer is improved by the reduced effective refractive index, and our measured EQE is consistent with this conventional model for thin-film LEDs. However, low absorption losses for modes guided in-plane may enable performance enhancement through photon recycling that allows outcoupling from these modes[30]. We anticipate the outstanding optoelectronic properties of the PPBH system to lead to low-cost and high-performance photon sources for lighting, display and communication technologies.

Methods

Synthesis of perovskite precursors

The synthesis of the NMAI was carried out in oven-dried glassware. All reagents and solvents were sourced from commercial suppliers (1-naphthylmethylamine: Aladdin, 98%; hydroiodic acid: Sigma-Aldrich, 99.99%, unstabilised; solvents: Honeywell, HPLC grade) and used as received. A solution of 1-naphthylmethylamine (2.575 g, 16 mmol, 1.0 equiv) in 50 mL tetrahydrofuran (THF) was cooled to 0 °C in an ice bath. Aqueous HI (4.4 g, 57 wt%, 19.6 mmol, 1.2 equiv) was added slowly and the reaction mixture was allowed to warm to room temperature over 2 h. After removing all volatiles with a rotary evaporator, the solids were rinsed with cold THF: dichloromethane (1:3, 20 mL). Repeated crystallization from boiling ethanol yielded the title compound as slightly yellowish needles (3.85 g, 13.43 mmol, 82 %). ^{1}H NMR (400 MHz, DMSO-d_6): δ 8.24 (s, 3H, NH_3), 8.16 (dd, J = 8.5, 1.1 Hz, 1H), 8.04 – 7.97 (m, 2H), 7.70 – 7.54 (m, 4H), 4.56 (s, 2H, CH_2). ^{13}C NMR (101 MHz, DMSO-d_6): δ 133.2, 130.6, 129.8, 129.2, 128.7, 127.3, 126.8, 126.3, 125.4, 123.4, 39.4.

Synthesis of MZO nanoparticles

The colloidal MZO nanocrystals were synthesized by a solution-precipitation process according to previously reported procedures with modifications[33]. Typically, zinc acetate dihydrate (296 mg) and magnesium acetate tetrahydrate (32.2 mg) was dissolved in dimethyl sulphoxide (DMSO) (15 mL) by stirring at room temperature. A solution of tetramethylammonium hydroxide (TMAH, 453 mg) in ethanol (5 mL) was then added dropwise to the metal salts solution. After reaction for 2 h, the product was decanted and purified twice with ethyl acetate and ethanol. Ethanol (6 mL) was added to disperse the final product and produce a colloidal MZO nanocrystal dispersion with a concentration of ~7 mg mL^{-1}. The MZO solution was filtered with a 0.45 μm PTFE filter before use.

Preparation of PPBH precursor solutions

The perovskite precursor was prepared by dissolving 41.72 mg NMAI, 25.17 mg FAI (Dyesol), 67.46 mg PbI_2 (TCI) and 33.54 mg poly-HEMA (Sigma-Aldrich) in 1 mL of anhydrous N,N-dimethylformamide (DMF) (Sigma-Aldrich). The precursor solution was stirred using a magnetic stir-bar for ~12 h at room temperature before use.

Fabrication of PPBH LEDs

Pre-patterned indium tin oxide (ITO) substrates (15 Ω/sq, Colorado Concept Coatings) were cleaned using ultrasonication in acetone and isopropanol for 15 min, respectively, and then dried with a

nitrogen blow gun, after which the substrates were treated under oxygen plasma etching (forward power: 300 W, reflected power: 0 W, 10 min). MZO nanoparticles were then deposited in air from the solution described previously to form a ~20-nm layer, and was annealed in a nitrogen environment at 150 ˚C for 10 min. Subsequently, a thin layer of PEIE[34] (~1 nm) was spin-coated from a 2-methoxyethanol (Sigma-Aldrich) solution, and annealed in air at 120 ˚C for 10 min. The perovskite was then deposited from the precursor in a nitrogen-filled glovebox to form a ~180-nm layer, followed by annealing at 100 ˚C for 5 min. On top of the perovskite film, a mixture of TFB and PFO (4:1 w/w) was spun from toluene solution to achieve a ~50-nm layer. Finally, 7 nm of MoO_x and 80 nm of gold were sequentially evaporated as top electrodes through a shadow mask at a pressure of 10^{-6} mBar. All devices were encapsulated with UV epoxy (NOA81, Thorlabs)/cover glass to avoid exposure to oxygen and moisture and degradation during measurement.

HR-TEM measurements

The TEM samples were prepared by gently scraping a PPBH layer with a carbon-coated copper grid. The high-resolution TEM images were obtained using a Tecnai F20 S/TEM system.

SEM measurements

Cross-section samples were fabricated by mechanical cutting using a diamond pen, and imaged in high-resolution scanning microscope (Hitachi S5500).

AFM measurements

The topographic images of the PPBH films on silicon substrates were obtained by AFM using a Digital Instruments Dimension 3100 microscope.

Grazing-incidence wide-angle X-ray scattering (GIWAXS) measurements

The GIWAXS patterns were collected at the XMaS beamline (ESRF, Grenoble). To monochromatise the X-ray beam coming from a bending magnet (E_c = 9.8 keV), a fixed-exit, water-cooled, double crystal Si(111) monochromator is used and is placed 25 m away from the source. The X-ray energy was tuned to 10 keV (1.2398 Å) with a flux of ~5 × 10^{10} photons s^{-1} at the sample position. The monochromatic beam was focused horizontally and vertically using a Rh-coated toroidal mirror, resulting in a 500 (horizontal) × 400 (vertical) μm^2 spot size at the sample position. To have a better-defined footprint in the vertical direction, a set of motorized slits (Huber, Germany) are employed immediately before the sample, resulting in a final beam spot size of 300 (horizontal) × 115 (vertical) μm^2. Diffraction patterns were collected at an out-of-plane incident angle of ~0.3°.

XRD measurements

X-ray diffraction (XRD) measurements were performed using Bruker D8 Discover and D8 Advance diffractometers with Ni-filtered Cu K_α radiation and a LynxEye position-sensitive detector. PPBH samples were deposited on silicon substrates. Crystal structure models were generated with the Accelrys Materials Studio software and optimized via Universal Force-Field simulations. Pawley refinements were carried out using the Materials Studio Reflex module.

Characterisation of LED performance

The current density-voltage (*J-V*) characteristics were measured using a Keithley 2400 source-meter unit. The photon flux was measured simultaneously using a calibrated silicon photodiodes centered over the LED. The radiance (in W sr^{-1} m^{-2}) of the devices were calculated based on the emission function of the PPBH LED and on the known spectral response of the silicon photodiode, and the external quantum efficiency (EQE) of the devices were calculated assuming a Lambertian profile[35,36]. The EL spectra of the devices were measured using a calibrated intensified CCD camera system (AndoriStar DH740 CCI-010) connected to a grating spectrometer (Andor SR303i). The accuracy of the spectral data was cross-checked against a Labsphere CDS-610 spectrometer. The LED measurement set-up has been previously cross-checked against a third-party industrial laboratory[16].

PLQE measurements

The steady-state absolute PLQE of PPBH samples were measured using an integrating sphere method[37]. A continuous-wave 532-nm diode laser with an excitation intensity of 10-300 mW cm^{-2} and a focused beam spot of ~0.3 mm^2 was used to excite the samples. The emission was measured using an Andor iDus DU490A InGaAs detector.

Besides, the excitation-intensity dependence of PLQE was further studied using 80-fs, 400-nm pulsed laser excitation (Supplementary Fig. 5c). The PL efficiency-excitation dependence, calculated by integrating the transient PL decay profiles measured under different excitation intensities, is generally understood by a competition between radiative recombination processes and non-radiative processes in 3D halide perovskites[28,29], according to Equations (1) and (2).

$$dn/dt = -an^k - bn^2 - (c_R + c_{NR})n \quad (1)$$

$$\eta(n) = \frac{bn^2 + c_R n}{an^k + bn^2 + (c_R + c_{NR})n} \quad (2)$$

where n is the excitation density, and the n^k term relates to a higher-order process such as Auger recombination (k = 3). a and b are the rate constants for the non-radiative k^{th}-order and radiative second-order (bimolecular) processes respectively. c_R and c_{NR} denote the radiative and non-radiative rate constants of the first-order term, respectively. η is the PLQE.

ns-µs transient photoluminescence measurements

The PPBH films for the PL measurements were spin-coated onto pre-cleaned fused silica substrates with the same method described in the device fabrication. The samples were then encapsulated with cover-slips and quick-drying epoxy. Time-resolved PL spectra were measured with an electrically-gated intensified CCD (iCCD) camera system (AndoriStar DH740 CCI-010) connected to a grating spectrometer (Andor SR303i). Photoexcitation was provided by femtosecond laser pulses which were generated in a custom-configured setup by second harmonic generation (SHG) in a BBO crystal from the fundamental output (pulse energy = 1.55 eV, pulse width = 80 fs) of a Ti:Sapphire laser system (Spectra-Physics Solstice). The laser pulses had photon energy of 3.1 eV (400 nm). The laser beam had an effective cross-sectional area of 0.2 mm^2 at its focal point, where the sample was positioned. A 420-nm long–pass filter was used to prevent scattered laser signal from entering the camera. Temporal evolution of the PL emission was obtained by stepping the iCCD gate delay with respect to the excitation pulse. The minimum gate width of the iCCD was ~2 ns.

Time-correlated single photon counting (TCSPC) measurements

The PPBH films spin-coated on pre-cleaned fused silica were photo-excited using a 407-nm pulsed laser with pulse width < 200 ps, at a repetition rate of 50 kHz-25 MHz. Photons emitted from the sample were detected by a Si-based single-photon avalanche photodiode. The instrument response function has a lifetime of ~0.2 ns. A 420-nm long-pass filter was used to screen-out any scattered laser signal in the optical path.

Transient electroluminescence measurements

The devices were electrically excited by a functional generator using 2-V square voltage pulses with a pulse width of 500 μs for the on-cycles (forward bias). The off-cycles of the device operation had a terminal voltage of 0 V (zero bias). The EL decay was recorded during the off-cycles of the pulses, with 50-ns time-steps. The instrument response time of the functional generator was ~10 ns. The transient EL of the devices was recorded using the same iCCD spectrometer adopted in the PL measurements. These measurement procedures and equipment employed were similar to what were used previously for transient EL characterisation of OLEDs[38,39], which did not appear to be RC limited; the EL decay processes with characteristic lifetimes of >50 ns (the temporal step size of the measurements) were reliably resolved.

Ultrafast (fs-ps) transient grating photoluminescence measurements

A Ti:Sapphire amplifier system (Spectra-Physics Solstice) operating at 1 KHz generating 80-fs pulses was split into the pump and probe beam arms. The pump beam was generated by second harmonic generation (SHG) in a BBO crystal and focused onto the sample. Photoluminescence was collimated using a silver off-axis parabolic mirror and focused onto the gate medium. About 80 μJ/pulse of the 800-nm laser output was used for the gate beams, which was first raised to 25 mm above the plane of the PL to produce a boxcar geometry and split into a pair of gate beams using a 50/50 beam splitter. The gate beams were focused onto the gate medium (fused silica), crossing at an angle of ~5° and overlapping with the focused PL. The two gate beams interfered and created a transient grating in the gate medium due to a modulation of the refractive index via the optical Kerr effect[16,40]. Temporal overlap between the two gate beams was achieved via a manual delay stage. The PL was then deflected on the transient grating causing a spatial separation of the gated signal from the PL background. Two lenses collimated and focused the gated signal onto the spectrometer entrance (Princeton Instruments SP 2150) after long- and short-pass filters removed the scattered pump and gate light, respectively. Gated PL spectra were measured using an intensified CCD camera (Princeton Instruments, PIMAX4). The (~10 ns) electronic shutter of the intensified CCD camera was used to further suppress long-lived PL background. PL spectra at each gate time delay were acquired from ~10000 laser shots. The time delay between pump and gate beams was controlled via a motorized optical delay line on the excitation beam path and a LabVIEW data acquisition program.

Transient absorption (TA) spectroscopy

The output of a Ti:Sapphire amplifier system (Spectra-Physics Solstice Ace) operating at 1 KHz and generating 80-fs pulses was split into the pump and probe beam paths. The visible broadband probe beam was generated in a home-built noncollinear optical parametric amplifier previously detailed[41].The 400-nm pump beam was created by sending the 800-nm fundamental beam of the

Solstice Ace through a second harmonic generating (SHG) beta barium borate (BBO) crystal of 1 mm thickness (Eksma Optics). The pump was blocked by a chopper wheel rotating at 500 Hz while a computer operated a mechanical delay stage (Newport) to adjust the delay between the pump and the probe. The transmitted pulses were collected with an InGaAs dual-line array detector (Hamamatsu G11608-512) driven and read out by a custom-built circuit board from Stresing Entwicklungsbüro.

Optical constant measurements

The optical properties of PPBH films and other solution-processed materials studied in this work were probed using a J.A. Woollam variable-angle spectroscopic ellipsometer. The data were fitted using a Cauchy model to extract the optical constants of the thin films.

Determination of perovskite/polymer volume fractions in PPBH films

To estimate the volume fractions of the perovskite and polymer phases in the PPBH, Lorentz-Lorenz relation (Equation (3)) was used.

$$\frac{n_m^2-1}{n_m^2+2}=v_1\left(\frac{n_1^2-1}{n_1^2+2}\right)+v_2\left(\frac{n_2^2-1}{n_2^2+2}\right) \quad (3)$$

where n_m is the refractive index of the mixed phase (PPBH), n_1 and n_2 are the refractive indices of the perovskite and polymer phases, respectively. v_1 and v_2 are the volume fractions of the two phases.

Using ellipsometry, the refractive indices of a PPBH film and an identically prepared quasi-2D/3D perovskite film without the polymer component are measured to be 1.9 and 2.1 (at 795 nm), respectively. The refractive index of the polymer, poly-HEMA, is 1.5[42]. The volume fractions, v_1 and v_2, are calculated to be 72% and 28% for the perovskite and polymer phases respectively.

Optical modelling of PPBH LEDs

To calculate the expected theoretical outcoupling, a transfer matrix thin-film interference model was constructed[43]. This model considers the outgoing wave power excited by a dipole source plane within a stack of uniform dielectric slabs of varying complex refractive index. Forwards and backward-going plane waves with a wavelength of 795 nm and varying in-plane wavevectors (or angles of emission) are excited by this dipole. Interference affects the total power radiated, but since we are interested in photon counts, we normalise by the total power a dipole emits at each location. We average over dipole orientation and polarizations, assuming uniform distribution of dipoles. The calculation assumes that the imaginary component of the refractive index of the emission layer is negligible[43,44]. While the code to implement this is written internally, it is constructed to be used in conjunction with the Moosh open-source framework[45] so that other tools from the Moosh toolbox can be used to investigate the same system. The thicknesses of layers are determined by SEM, and the refractive indices are either measured using ellipsometry or from literature values (Supplementary Table 2).

Very little power escapes through the gold layer, and outcoupled power is primarily delivered through the glass-substrate side. The remaining power may be assigned to one of several different classes depending on the in-plane wavevector, k_x. For values of k_x below the total free-space wavevector, k_{free} (equivalently, with angles of emission below the escape angle), power that does not escape is classified as 'absorbed'. Physically, the remaining power is also absorbed within the system, but had no prospect of escape. We therefore divide this into three groups: light with $k_{free} < k_x <$

$n_{subs}k_{free}$ is considered trapped by the substrate glass later, with refractive index n_{subs} = 1.5. Light with $k_{free}n_{subs} < k_x < n_{source}k_{free}$ is considered waveguided along the PPBH emissive (source) layer, with refractive index n_{source} = 1.9, and light with $k_x > n_{source}k_{free}$, i.e. emitted at an imaginary angle, is channeled into plasmons in the metal layer.

Lateral photoluminescence experiments

Lateral PL measurements were acquired using a confocal microscope (WITec Alpha RAS system). A 405-nm CW laser (Coherent CUBE) was coupled into the microscope using optical fiber. The excitation laser was focused onto the sample (PPBH side) using a 40× objective. The average power of the laser at its focal point was 0.5 μW. The PL of the sample was collected in the transmission geometry (silica substrate side) using a 60× objective. The collection objective was mounted on an XYZ translation stage (piezo-electric) and moved laterally in 1-μm steps away from the localised laser excitation spot. The collected signal was detected using a spectrometer fitted with a Si-CCD array detector (Andor iDus BR-DD). The excitation component of the transmitted light (405 nm) was blocked using a long-pass filter with a cut-off wavelength of 435 nm. All movements of the stage and lenses (1D lateral PL and 2D PL mapping) were automated and controlled by the WITec ScanCtr spectroscopy Plus software. All PL spectra were averaged 10 times during the acquisition process. All measurements were performed in a N_2 atmosphere.

Data availability. The data that support the plots within this paper and other findings of this study are available in the University of Cambridge Repository (www.repository.cam.ac.uk). Related research results are available from the corresponding authors upon reasonable request.

References

1. Kojima, A., Teshima, K., Shirai, Y. & Miyasaka, T. Organometal halide perovskites as visible-light sensitizers for photovoltaic cells. *J. Am. Chem. Soc.* **131,** 6050–6051 (2009).
2. Lee, M. M., Teuscher, J., Miyasaka, T., Murakami, T. N. & Snaith, H. J. Efficient hybrid solar cells based on meso-superstructured organometal halide perovskites. *Science* **338,** 643–647 (2012).
3. Kim, H.-S. *et al.* Lead iodide perovskite sensitized all-solid-state submicron thin film mesoscopic solar cell with efficiency exceeding 9%. *Sci. Rep.* **2,** 591 (2012).
4. Green, M. A., Ho-Baillie, A. & Snaith, H. J. The emergence of perovskite solar cells. *Nat. Photonics* **8,** 506–514 (2014).
5. Tan, Z.-K. *et al.* Bright light-emitting diodes based on organometal halide perovskite. *Nat. Nanotechnol.* **9,** 687–692 (2014).
6. Cho, H. *et al.* Overcoming the electroluminescence efficiency limitations of perovskite light-emitting diodes. *Science* **350,** 1222–1225 (2015).
7. Yuan, M. *et al.* Perovskite energy funnels for efficient light-emitting diodes. *Nat. Nanotechnol.* **11,** 872–877 (2016).
8. Wang, N. *et al.* Perovskite light-emitting diodes based on solution-processed self-organized multiple quantum wells. *Nat. Photonics* **10,** 699–704 (2016).
9. Deschler, F. *et al.* High photoluminescence efficiency and optically pumped lasing in solution-processed mixed halide perovskite semiconductors. *J. Phys. Chem. Lett.* **5,** 1421–

1426 (2014).
10. Xing, G. *et al.* Low-temperature solution-processed wavelength-tunable perovskites for lasing. *Nat. Mater.* **13,** 476–480 (2014).
11. Dou, L. *et al.* Solution-processed hybrid perovskite photodetectors with high detectivity. *Nat. Commun.* **5,** 5404 (2014).
12. Fang, Y., Dong, Q., Shao, Y., Yuan, Y. & Huang, J. Highly narrowband perovskite single-crystal photodetectors enabled by surface-charge recombination. *Nat. Photonics* **9,** 679–686 (2015).
13. Yang, X. *et al.* Efficient green light-emitting diodes based on quasi-two-dimensional composition and phase engineered perovskite with surface passivation. *Nat. Commun.* **9,** 570 (2018).
14. Reineke, S. *et al.* White organic light-emitting diodes with fluorescent tube efficiency. *Nature* **459,** 234–238 (2009).
15. Uoyama, H., Goushi, K., Shizu, K., Nomura, H. & Adachi, C. Highly efficient organic light-emitting diodes from delayed fluorescence. *Nature* **492,** 234–238 (2012).
16. Di, D. *et al.* High-performance light-emitting diodes based on carbene-metal-amides. *Science* **356,** 159–163 (2017).
17. Ball, J. M. & Petrozza, A. Defects in perovskite-halides and their effects in solar cells. *Nat. Energy* **1,** 16149 (2016).
18. Ross, R. T. Some thermodynamics of photochemical systems. *J. Chem. Phys.* **46,** 4590–4593 (1967).
19. Shockley, W. & Queisser, H. J. Detailed balance limit of efficiency of p-n junction solar cells. *J. Appl. Phys.* **32,** 510–519 (1961).
20. Yablonovitch, E. Lead halides join the top optoelectronic league. *Science* **351,** 1401 (2016).
21. Di, D. *et al.* Size-dependent photon emission from organometal halide perovskite nanocrystals embedded in an organic matrix. *J. Phys. Chem. Lett.* **6,** 446–450 (2015).
22. Li, G. *et al.* Efficient light-emitting diodes based on nanocrystalline perovskite in a dielectric polymer matrix. *Nano Lett.* **15,** 2640–2644 (2015).
23. Xiao, Z. *et al.* Efficient perovskite light-emitting diodes featuring nanometre-sized crystallites. *Nat. Photonics* **11,** 108–115 (2017).
24. Weller, M. T., Weber, O. J., Frost, J. M. & Walsh, A. Cubic perovskite structure of black formamidinium lead iodide, α-$[HC(NH_2)_2]PbI_3$, at 298 K. *J. Phys. Chem. Lett.* **6,** 3209–3212 (2015).
25. Wang, J. *et al.* Interfacial control toward efficient and low-voltage perovskite light-emitting diodes. *Adv. Mater.* **27,** 2311–2316 (2015).
26. Dai, X. *et al.* Solution-processed, high-performance light-emitting diodes based on quantum dots. *Nature* **515,** 96–99 (2014).
27. Yang, Y. *et al.* Top and bottom surfaces limit carrier lifetime in lead iodide perovskite films. *Nat. Energy* **2,** 16207 (2017).
28. Saba, M. *et al.* Correlated electron–hole plasma in organometal perovskites. *Nat. Commun.* **5,** 5049 (2014).
29. Richter, J. M. *et al.* Enhancing photoluminescence yields in lead halide perovskites by photon recycling and light out-coupling. *Nat. Commun.* **7,** 13941 (2016).
30. Pazos-Outón, L. M. *et al.* Photon recycling in lead iodide perovskite solar cells. *Science* **351,**

1430–1433 (2016).
31. Shi, D. *et al.* Low trap-state density and long carrier diffusion in organolead trihalide perovskite single crystals. *Science* **347,** 519–522 (2015).
32. Brenner, T. M., Egger, D. A., Kronik, L., Hodes, G. & Cahen, D. Hybrid organic-inorganic perovskites: low-cost semiconductors with intriguing charge-transport properties. *Nat. Rev. Mater.* **1,** 15007 (2016).
33. Bai, S. *et al.* High-performance planar heterojunction perovskite solar cells: preserving long charge carrier diffusion lengths and interfacial engineering. *Nano Res.* **7,** 1749–1758 (2014).
34. Zhou, Y. *et al.* A universal method to produce low-work function electrodes for organic electronics. *Science* **336,** 327–332 (2012).
35. Greenham, N. C., Friend, R. H. & Bradley, D. D. C. Angular dependence of the emission from a conjugated polymer light-emitting diode: implications for efficiency calculations. *Adv. Mater.* **6,** 491–494 (1994).
36. Forrest, S. R., Bradley, D. D. C. & Thompson, M. E. Measuring the efficiency of organic light-emitting devices. *Adv. Mater.* **15,** 1043–1048 (2003).
37. de Mello, J. C., Wittmann, H. F. & Friend, R. H. An improved experimental determination of external photoluminescence quantum efficiency. *Adv. Mater.* **9,** 230–232 (1997).
38. Di, D. *et al.* Efficient triplet exciton fusion in molecularly doped polymer light-emitting diodes. *Adv. Mater.* **29,** 1605987 (2017).
39. Wallikewitz, B. H., Kabra, D., Gélinas, S. & Friend, R. H. Triplet dynamics in fluorescent polymer light-emitting diodes. *Phys. Rev. B* **85,** 45209 (2012).
40. Chen, K., Gallaher, J. K., Barker, A. J. & Hodgkiss, J. M. Transient grating photoluminescence spectroscopy: an ultrafast method of gating broadband spectra. *J. Phys. Chem. Lett.* **5,** 1732–1737 (2014).
41. Jakowetz, A. C. *et al.* What controls the rate of ultrafast charge transfer and charge separation efficiency in organic photovoltaic blends. *J. Am. Chem. Soc.* **138,** 11672–11679 (2016).
42. Xu, X, Goponenko, A. V., & Asher, S. A. Polymerized polyHEMA photonic crystals: pH and ethanol sensor materials. *J. Am. Chem. Soc.* **130,** 3113-3119 (2008).
43. Neyts, K. A. Simulation of light emission from thin-film microcavities. *J. Opt. Soc. Am. A* **15,** 962 (1998).
44. Benisty, H., Stanley, R. & Mayer, M. Method of source terms for dipole emission modification in modes of arbitrary planar structures. *J. Opt. Soc. Am. A* **15,** 1192 (1998).
45. Defrance, J. *et al.* Moosh: a numerical swiss army knife for the optics of multilayers in Octave/Matlab. *J. Open Res. Softw.* **4,** (2016).

Acknowledgements

B.Z. thanks the Cambridge Trust and China Scholarship Council for funding and support. S.B. is supported by a VINNMER Marie-Curie Fellowship. R.S. acknowledges the Royal Society Newton-Bhabha International Fellowship. M.A. acknowledges the President of the UAE's Distinguished Student Scholarship Program (DSS), granted by the UAE's Ministry of Presidential Affairs. XMaS is a mid-range facility supported by the Engineering and Physical Sciences Research Council (EPSRC). We are grateful to all the XMaS beamline team staff for their support. P.G. acknowledges the 'Thousand Talent Program' for support. D.D. and R.H.F. acknowledge the EPSRC for support. The research leading to these results has received funding from the European Research

Council (ERC) under the European Union's Horizon 2020 research and innovation programme (grant agreement no. 670405).

Author contributions

B.Z. and D.D. developed and characterised the high-efficiency LEDs. D.D., B.Z. and L.Y. carried out the ns-μs transient PL and EL studies. V.K. conducted the transient absorption experiments. J.M.R. performed the fs-ps transient PL measurements. R.L. developed the optical model for the LED devices under the guidance of N.C.G. S.B. synthesised the MZO nanocrystals, tailored the MZO properties and contributed to the LED development. R.S. carried out the lateral PL experiments. F.A., L.L. and P.G. synthesized the perovskite precursors. L.D. performed the HR-TEM and AFM measurements. X.-J.S. and B.Z. performed the SEM studies. F.A., M.A., P.G. and B.Z. carried out the XRD analysis. J.Z. helped with some transient measurements and PLQE calculations. D.D. and B.Z. analysed all the results and wrote the manuscript which was revised by R.H.F. All authors contributed to the work and commented on the paper. D.D. planned the project and guided the work, with R.H.F.

Competing financial interests

R.H.F., H.J.S. and N.C.G. are co-founders of Heliochrome Ltd.

Corresponding authors

Correspondence to: Richard H. Friend (rhf10@cam.ac.uk) or Dawei Di (dd403@cam.ac.uk).

Supplementary Information for:

High-efficiency perovskite-polymer bulk heterostructure light-emitting diodes

Baodan Zhao[1], Sai Bai[2,3], Vincent Kim[1], Robin Lamboll[1], Ravichandran Shivanna[1], Florian Auras[1], Johannes M. Richter[1], Le Yang[1,4], Linjie Dai[1], Mejd Alsari[1], Xiaojian She[1], Lusheng Liang[5], Jiangbin Zhang[1], Samuele Lilliu[6,7], Peng Gao[5], Henry J. Snaith[2], Jianpu Wang[8], Neil C. Greenham[1], Richard H. Friend[1]* & Dawei Di[1]*

9. Cavendish Laboratory, Cambridge University, J. J. Thomson Avenue, Cambridge, CB3 0HE, UK
10. Department of Physics, University of Oxford, Clarendon Laboratory, Oxford, OX1 3PU, UK
11. Department of Physics, Chemistry and Biology (IFM), Linköping University, Linköping, SE-581 83, Sweden
12. Institute of Materials Research and Engineering (IMRE), Agency for Science, Technology and Research (A*STAR), 2 Fusionopolis Way, Singapore 138634, Singapore
13. Laboratory of Advanced Functional Materials, Xiamen Institute of Rare Earth Materials, Haixi Institute, Chinese Academy of Sciences, Xiamen 361021, China
14. Department of Physics and Astronomy, University of Sheffield, Sheffield, S3 7RH, UK
15. The UAE Centre for Crystallography, United Arab Emirates
16. Institute of Advanced Materials (IAM), Nanjing Tech University, 30 South Puzhu Road, Nanjing, 211816, China

*Corresponding author. E-mail: dd403@cam.ac.uk (D.D.); rhf10@cam.ac.uk (R.H.F.).

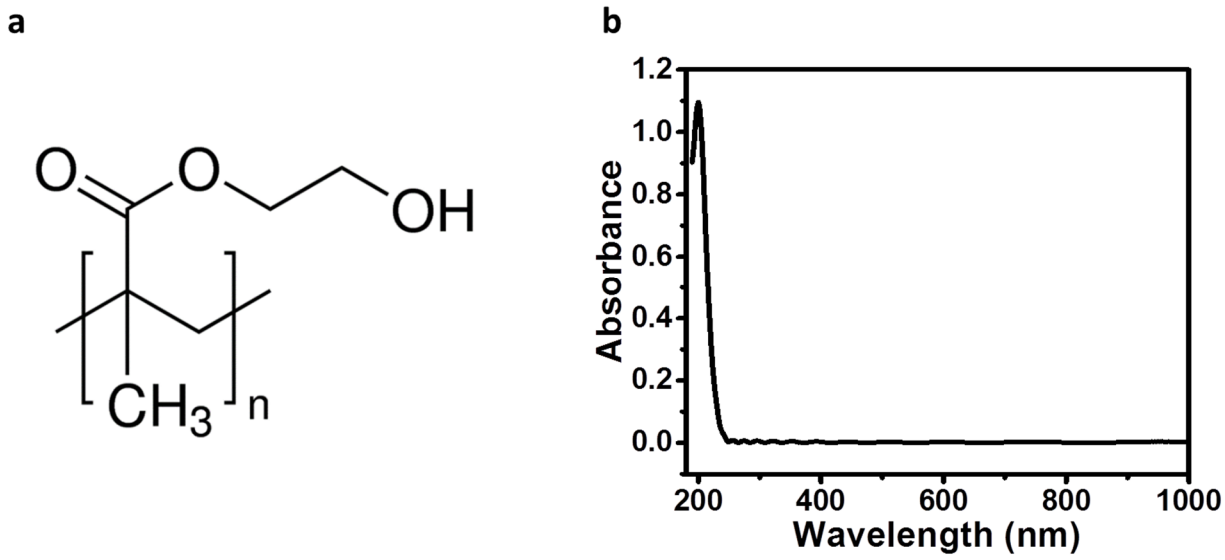

Figure S1 | Further details of poly-HEMA. a, Chemical structure. **b**, UV-Vis absorbance of poly-HEMA, showing an optical bandgap of ~4.96 eV.

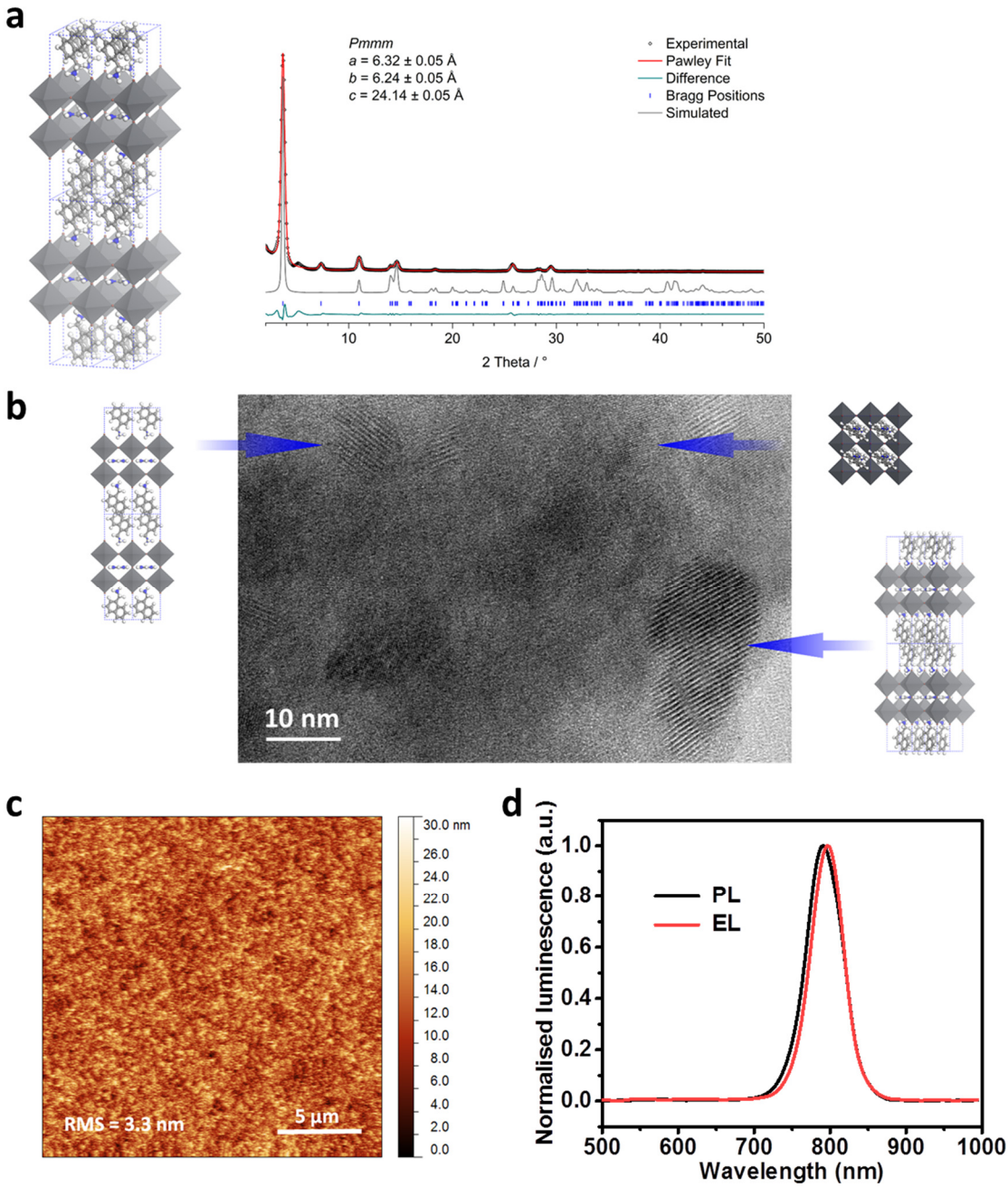

Figure S2 | Further material characterisation of the PPBH film. a, Experimental XRD pattern of the PPBH film (black dots). Pawley refinement (red line) using the force-field optimised structure model shown on the left reproduces the experimental data very well and confirms that the crystalline regions of the films consist almost exclusively of the quasi-2D $(NMA)_2(FA)Pb_2I_7$ phase (grey). For clarity, only one of the respective symmetry-equivalent orientations of the organic cations is displayed. The broadened reflection at 5° might indicate the presence of a small 2D $(NMA)_2PbI_4$ impurity. Scherrer analysis on the reflections at 3.6° and 11.0° reveals average crystallite sizes of 55 nm and 30 nm, respectively. **b**, High-resolution TEM image showing $(NMA)_2(FA)Pb_2I_7$ crystallites in different orientations. **c**, AFM image of the PPBH film, showing an RMS roughness of 3.3 nm. **d**, PL and EL spectra of the PPBH.

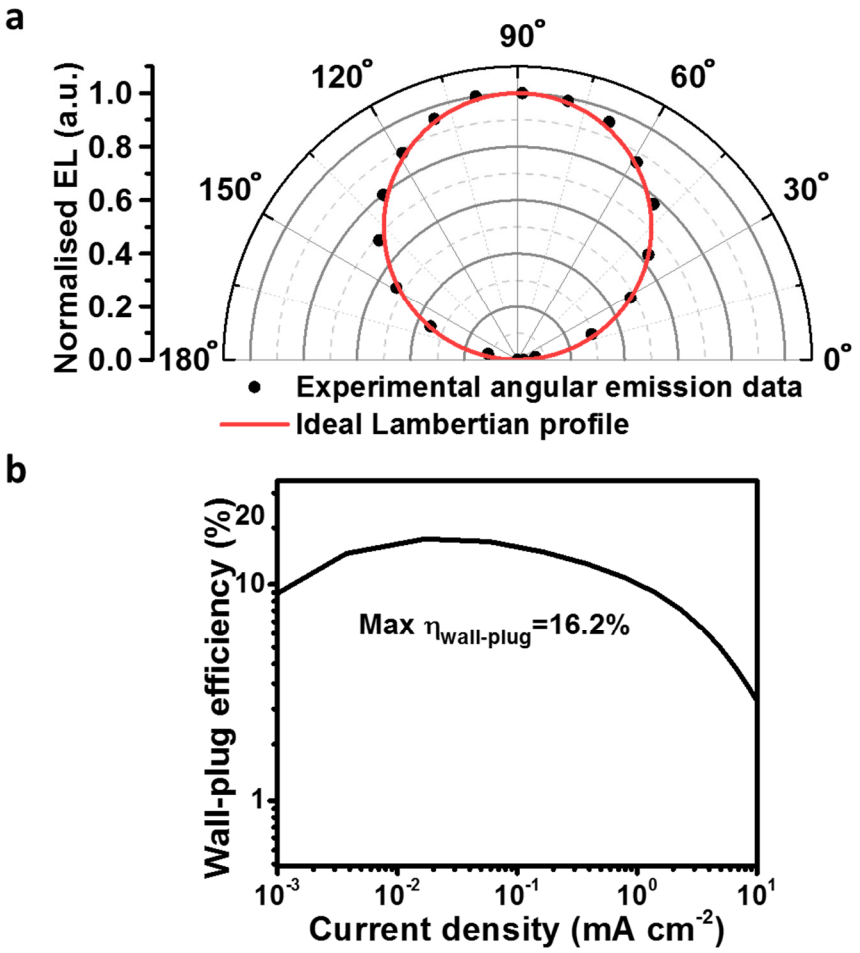

Figure S3 | Additional LED data. a, Angular emission profile of a PPBH LED. **b**, Wall-plug efficiency (electricity-to-light power-conversion efficiency) of the best PPBH LED.

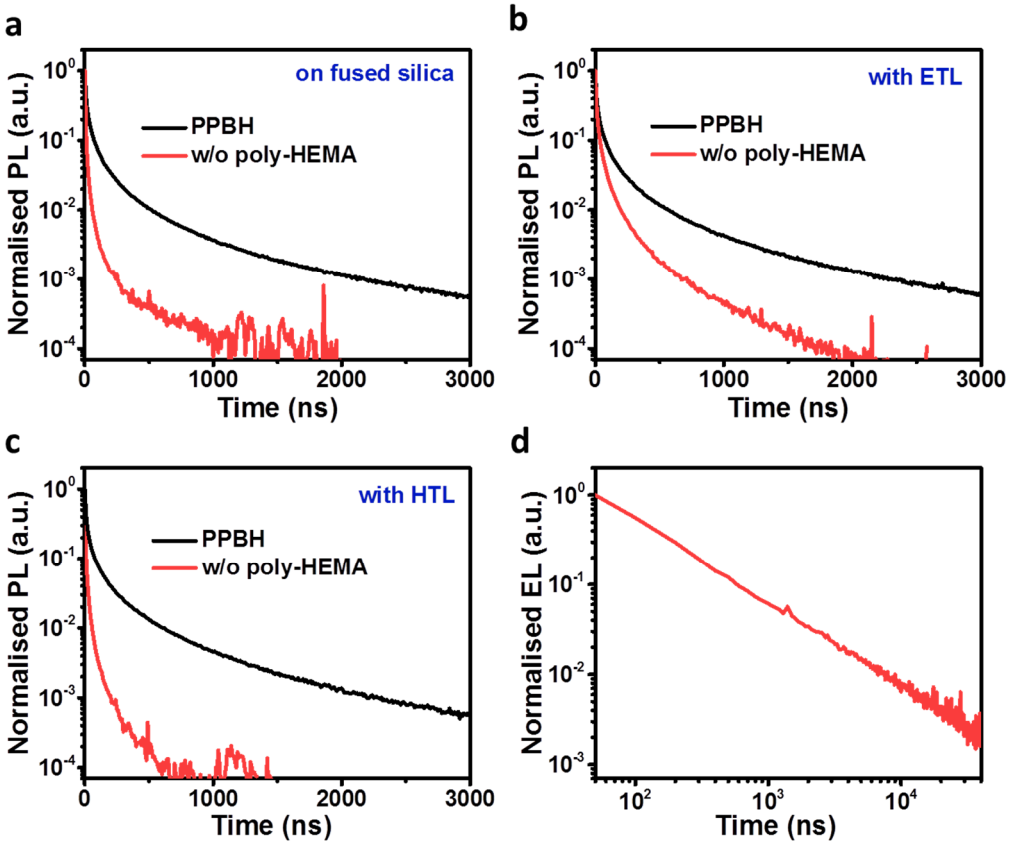

Figure S4 | Charge-transport-interface-dependent transient luminescence data. a-c, PL decay kinetics of PPBH films and identically-prepared quasi-2D/3D perovskite films without the poly-HEMA polymer component in contact with different materials; **a**, on fused silica substrates (without charge-transport layers); **b**, with electron-transport layer (ETL); **c**, with hole-transport layer (HTL). For the PL measurements, the excitation source was a 400-nm, 80-fs pulsed laser with a repetition frequency of 1 kHz. The excitation fluence was 5 μJ cm^{-2}. **d**, Transient EL measurements of a PPBH LED. During the transient EL measurements, the device was driven by 2 V/0 V (on/off) square voltage pulses at a frequency of 1 kHz. The EL decay was recorded during the off-cycles of the pulses, with 50-ns time-steps. It should be noted that the transient EL kinetics can be influenced by other processes such as the measurement circuit RC discharge rate, and the transit time of the slower carriers.

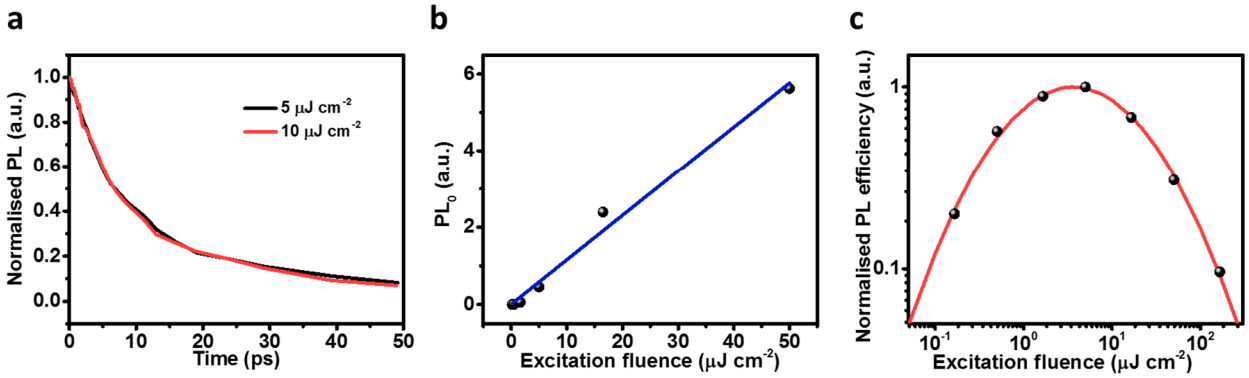

Figure S5 | Further PL data collected using fs laser excitation. a, Ultrafast (fs-ps) PL decay kinetics of the PPBH at 550-620 nm. **b**, Initial PL intensity (PL counts at $t \approx 0$ ns), as a function of excitation fluence. **c**, Fluence-dependent PL efficiency of the PPBH film. For these measurements, the excitation source was a 400-nm, 80-fs pulsed laser with a repetition frequency of 1 kHz.

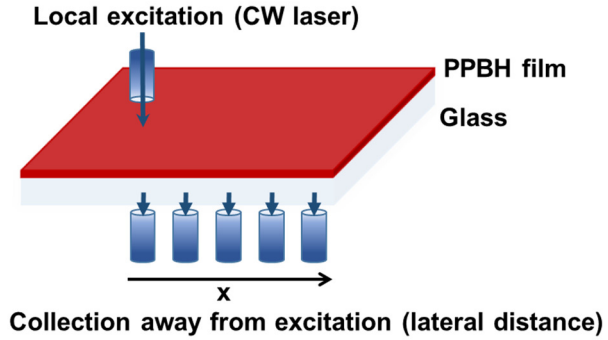

Figure S6 | Lateral PL experimental setup.

Table S1 | Photophysical parameters extracted from various transient optical measurements of the PPBH system. 'Excitation transfer' denotes the ultrafast migration of localised higher-energy excitations from the quasi-2D perovskite $(NMA)_2(FA)Pb_2I_7$ to delocalised lower-energy excitations (charges) on the quasi-3D perovskite sites, characterised using the TA experiments. 'Early-time (fs-ps) PL decay' is the initial PL decay kinetics observed in the quasi-2D perovskite $(NMA)_2(FA)Pb_2I_7$, measured using the fs-ps ultrafast PL setup. 'Bimolecular' denotes the bimolecular (band-to-band) radiative recombination processes in the quasi-3D perovskite domains, characterised using the ns-µs transient PL setup. 'Monomolecular' stands for the first-order (exponential) decay processes observed from the ns-µs PL decay tail kinetics. k and τ represent the rate constant and lifetime of each process, respectively.

Excitation transfer (quasi-2D/3D)		**Early-time (fs-ps) PL decay (quasi-2D)**		**Bimolecular (quasi-3D)**	**Monomolecular (quasi-3D)**	
Transient absorption		Ultrafast (fs-ps) transient PL		ns-µs transient PL	ns-µs transient PL	
k (s^{-1})	τ (s)	k (s^{-1})	τ (s)	k ($cm^3\ s^{-1}$)	k (s^{-1})	τ (s)
1.0×10^{12}	1.0×10^{-12}	1.0×10^{11}	1.0×10^{-11}	3.2×10^{-11}	6.7×10^{5}	1.5×10^{-6}

Table S2 | Parameters for optical modelling.

Layer	Thickness (nm)	Refractive index (~795 nm)
Air	-	1
Au	80	0.124+5.009i
TFB-PFO/MoO_x	57	1.57+0.04i
PPBH	180	1.9
MZO/PEIE	20	1.9
ITO	150	1.61+0.0056i
Glass	1×10^6	1.5
Air	-	1